

Ricker wavelet deconvolution of Western Australia data in the radial/time domain

Taylor Dahlke and Jon Claerbout

ABSTRACT

Performing deconvolution in the radial-time ($r=x/t,t$) domain is a method more consistent with the theory of the standard convolutional model than is deconvolution in the offset-time (x,t) domain. In this work we transform marine 2D seismic line data into the (r,t) domain, perform deconvolution along each common velocity panel, and transform back to the (x,t) domain. We also perform deconvolution on the same data (with no transform) along each common-offset panel in the (x,t) domain for comparison. Comparing in the (x,t) domain shows us that only limited differences in illumination are accomplished, even at far offset. Analysis of the spectra also shows us similar source and receiver frequency notches in the wavelet extracted from the data using both types of deconvolution.

INTRODUCTION

An important objective in seismic imaging is to remove the acquisition response from our data so that the underlying earth response can be more clearly observed and interpreted. Deconvolution is the process of extracting the source wavelet from the data in order to reach this objective. While it has been common practice to perform deconvolution for a minimum phase wavelet, it has been shown to be both possible and beneficial to extract a Ricker source wavelet instead, so as to better match the ghosting phenomenon that is associated with marine seismic acquisition (Zhang, 2011). One problem that must be addressed is the non-stationarity of the source wavelet along the time axis when in the offset-time (x,t) domain. This non-stationarity occurs because of geometric spreading as well as attenuation along the raypath, which depends on parameters such as length of the raypath through different layers, and the spectrum change with angle caused by the ghost delay changing with angle.

Regardless, the non-stationarity of a source wavelet produces a time-variant spectrum (TVS) (Margrave, 1997). Methods to account for the time variance of the spectrum in deconvolution (such as windowing in time) can be computationally expensive, and can create “stitching” artifacts from recombining data windows into a final image. In this paper we demonstrate that the raypaths represented by each trace in the radial-time ($r=x/t,t$) domain have similar path lengths in each layer and similar angles of incidence, which means the attenuation along each trace is causal,

rather than non-linear as in the (x,t) domain. The causal case is closer to the standard convolutional model, and performing deconvolution on the data in the (r,t) domain should result in the extraction of a better effective source wavelet. In this paper we will demonstrate how performing deconvolution in the (r,t) domain better fits the assumptions of the standard convolutional model. Next we will discuss the pre-processing and deconvolution methods that we used. Last we will show the results of deconvolution in the (r,t) domain, and compare with the results of performing deconvolution on common-offset images in the (x,t) domain.

(r,t) Domain

Most forms of deconvolution arise from the assumptions in the standard convolutional model. This model is one-dimensional and assumes that seismic energy is transmitted along a single raypath and strikes reflectors at a normal incidence angle. These assumptions are regularly violated because of the constraints and realities of acquisition. Performing deconvolution in the (x,t) domain largely ignores these assumptions, with the raypath from each reflector varying widely in take-off angle and path length within each reflector bed. By converting to the (r,t) domain, the seismic energy in each trace shares a common down-going raypath, and the upward reflections travel parallel to each other within reflector beds (Figure 1). Furthermore, the take-off angles are the same for each reflector. The (r,t) domain geometry better satisfies the standard convolutional model assumptions, with the only true difference being that the upward raypath does not follow the original path of the downward raypath (Henyey, 2004). However, assuming flat and horizontally uniform geology, we can think of the rays as following a common raypath, since the incidence angle and path length through each layer is the same. It should be noted that Figure 2 shows a case where the velocity varies with depth. For this paper our transform of $r = x/t$ assumes a constant velocity and ignores slant stacking, in order to take account of only the first order effects of the radial transform (Figure 1).

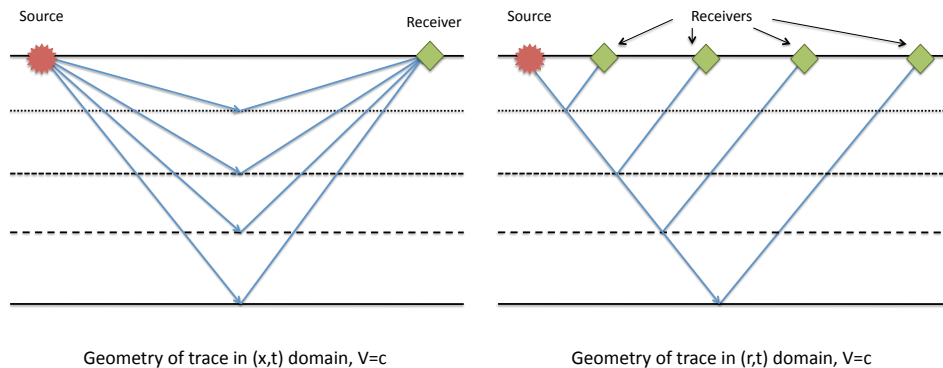


Figure 1: Diagram of raypath geometries in (x,t) and (r,t) domains. Constant velocity. [NR]

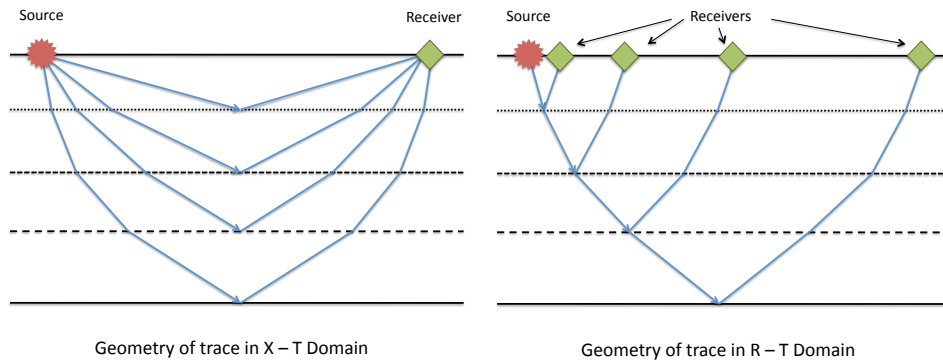


Figure 2: Diagram of raypath geometries in (x,t) and (r,t) domains. Velocity varies with depth only. [NR]

Ricker Wavelet

Marine data is typically collected using an air-gun source coupled with a receiver array that is towed at some depth below the water surface. While the source wavelet is often approximated as a Gaussian impulse, the wavelet recorded at the receiver is aggregated from this impulse reflection following four different ray paths. These ray paths include one direct reflection off the water bottom, one source and one receiver ghost reflection, and one double ghost reflection. These four reflections are superimposed, and the resulting pressure signal is captured at the receiver as a (opposite phase) Ricker wavelet (Liner, 2004).

While Figure 3 shows different ocean-bottom reflection points for the source ghost and receiver ghost, these reflection points are approximately the same for all four ray-paths when the ocean depth is much larger than the source/receiver depth. For this reason, the source and receiver ghost signals can be summed constructively, creating the main lobe of the superimposed wavelet observed at the receiver. Since the ghost reflections have opposite phase from the source impulse (due to the high impedance contrast at the water surface), these reflections destructively interfere with certain frequencies that depend on the depth of the streamer from the water surface. Notches are visible in the frequency spectra at the interference frequencies. These notch frequencies can be calculated with the following equation:

$$f_c = \frac{nc}{2z_c \cos \Theta}, \quad (1)$$

where z_c is the depth of the streamer, Θ is the direction of wave propagation from a reflection point (relative to the vertical), c is the velocity of the water, and n is an integer value. The information gathered from the observer's log of the survey data used in this paper indicates that the source depth was 5 m with ± 0.5 m as an acceptable variance, while the receiver depth was recorded as varying from 6.2 - 7.4

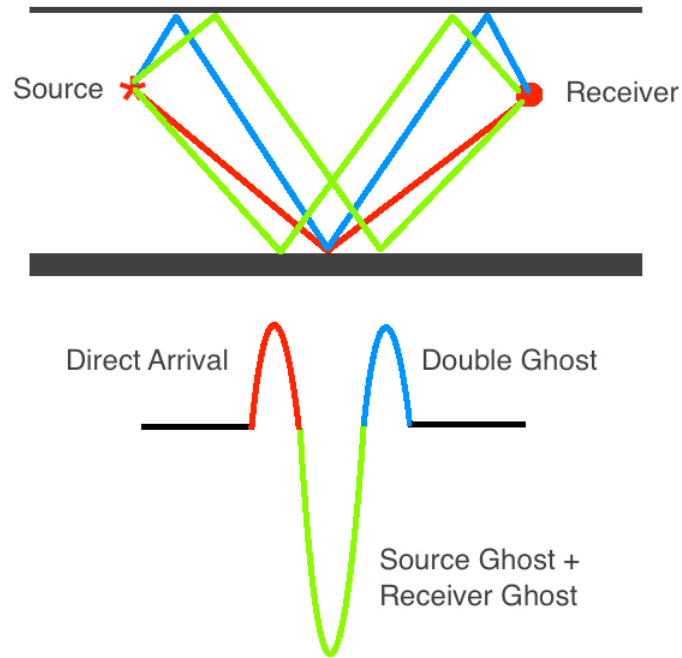


Figure 3: Diagram of Ricker wavelet construction. [NR]

m. Using equation (1), we found that the expected frequency notches at zero offset would range between 101 and 121 Hz for the receiver notch, and between 136 and 167 Hz for the source notch.

Deconvolution

The purpose of deconvolution is to separate the components of data due to acquisition effects from the components of the data that represent the response of the earth (Guitton, 2012). This requires that we create a filter that can perform this separation (Barak, 2012). When deconvolution is performed at increasing offset, the frequency notching from the ghost reflections influences the spectra of the source wavelet produced by our deconvolution (Figures 6(a) and 6(b)). Given our data $D(w)$, the deconvolved output can be defined as:

$$r_t = FT^{-1} \left[D_w e^{\sum_t u_t Z^t} \right], \quad (2)$$

where $u_t = \log$ spectrum variables, and $Z = e^{i\omega}$.

The method of deconvolution used on this data creates a filter based on parameters that act on the “lag-log” axis, as described by Claerbout (2013). If we begin with

a wavelet $W(\omega)$ in the frequency domain, as defined using equations (3), (4) and (5) below, then we can derive equation (6) (where N is a positive integer), which describes the wavelet in the lag-log domain:

$$W(\omega) = e^{U(\omega)} \quad (3)$$

$$U(\omega) = \sum_{\tau=0}^{2048} u_{\tau} Z^{\tau} \quad (4)$$

$$Z = e^{i\omega\Delta t} \quad (5)$$

$$W(\tau) = \exp \left(\sum_{\tau=0}^{2^N} u_{\tau} Z^{\tau} \right). \quad (6)$$

This representation of the wavelet allows us to conceptually divide $W(\omega)$ into a composite of three wavelets, each defined by a range along the lag-log axis τ . The physical representation of these three wavelets can be thought of as:

$$e^{(A+B+C)} = e^A e^B e^C \quad (7)$$

$$e^{\sum_{\tau=1}^{2048} u_{\tau} Z^{\tau}} = e^{\sum_1^5} e^{\sum_6^{30}} e^{\sum_{31}^{2048}} \quad (8)$$

$$\text{wavelet} = (\text{continuity})(\text{Ricker})(\text{bubble}) \quad (9)$$

APPLICATION TO WESTERN AUSTRALIA DATA

The Chevron Western Australia data set that we deconvolved was collected from a marine 2D line survey, in about 950 m of water. Just over seven seconds of data with two-millisecond sampling was recorded for each of the 564 offset locations, each with a spacing of 12.5 m. In total, 1810 shots were recorded.

Preprocessing

Because of the high levels of sea-swell noise in the original data, one of the preprocessing steps was velocity filtering (Figure 4). A velocity filter is a far more appropriate method of eliminating this noise than a low-cut frequency filter, which would eliminate the sea-swell as well as compromise desirable components of the signal spectrum. The velocity filter we used was designed to mute all events that had a move-out velocity lower than the acoustic speed of salt water (1500 m/s). The filter also implemented a transition zone from the mute region of the velocity space, which was necessary to suppress the edge artifacts that occur when the filter has a hard “zero-to-one” filter boundary. This soft transition extended from the slope edge along the ω axis away from the origin, in order to preserve the zero weight at “zero” frequency.

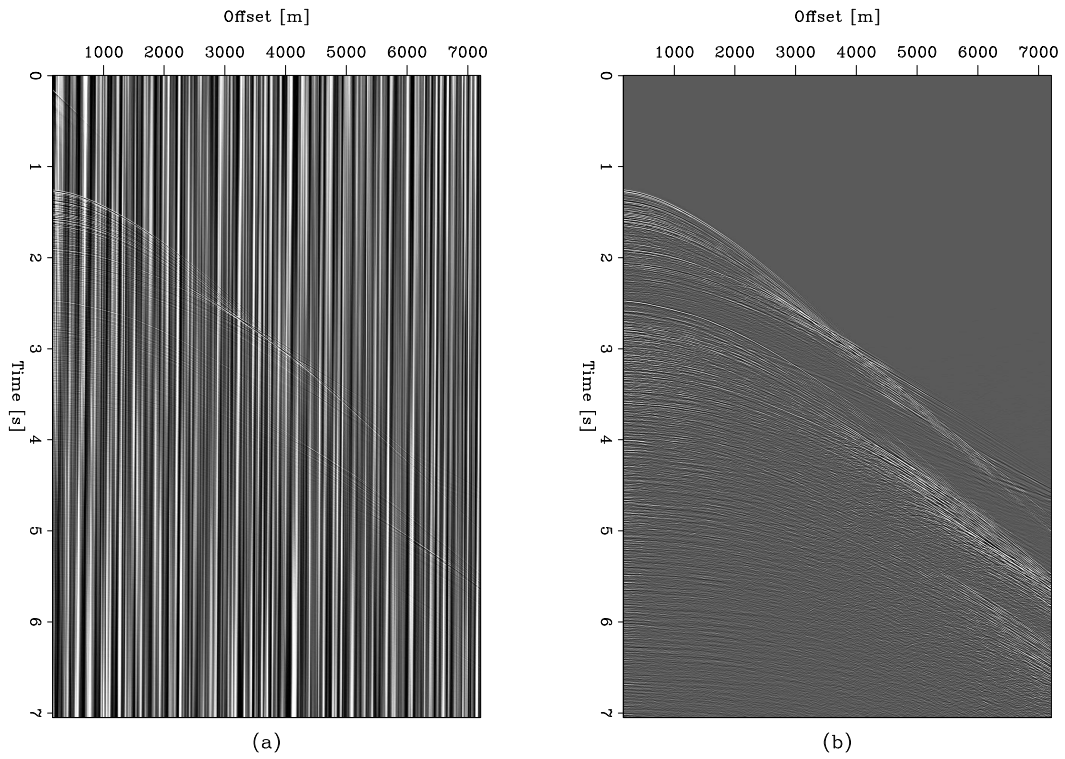


Figure 4: (a) Raw data input. (b) Velocity-filtered data. [ER]

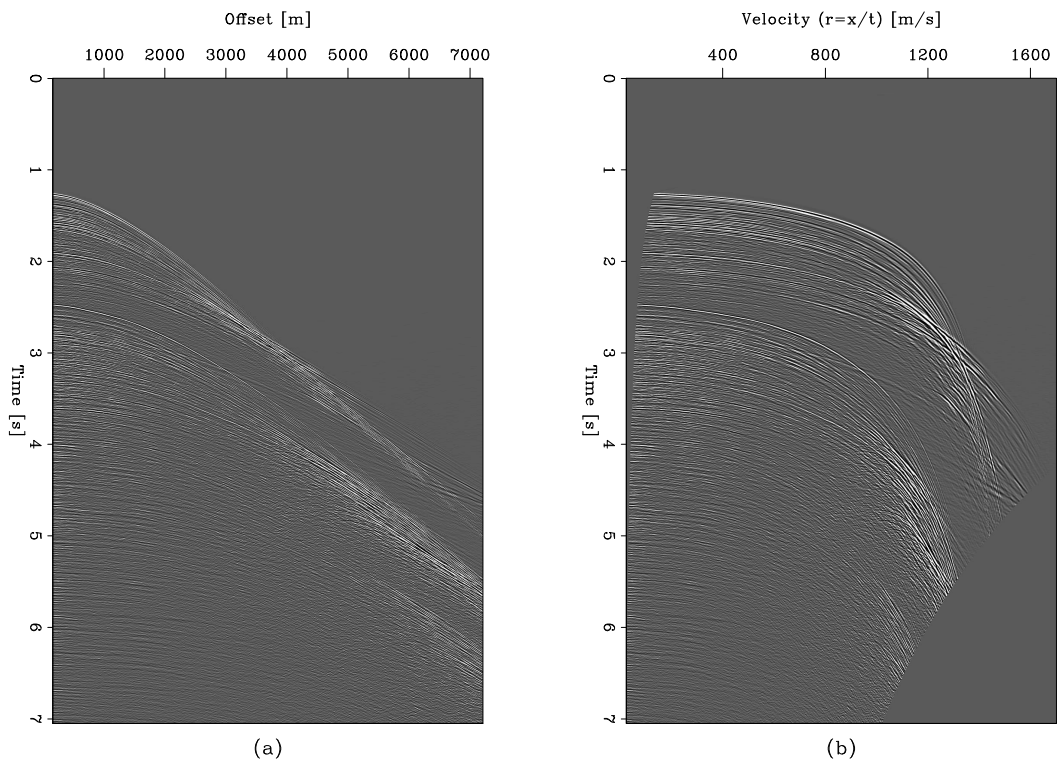
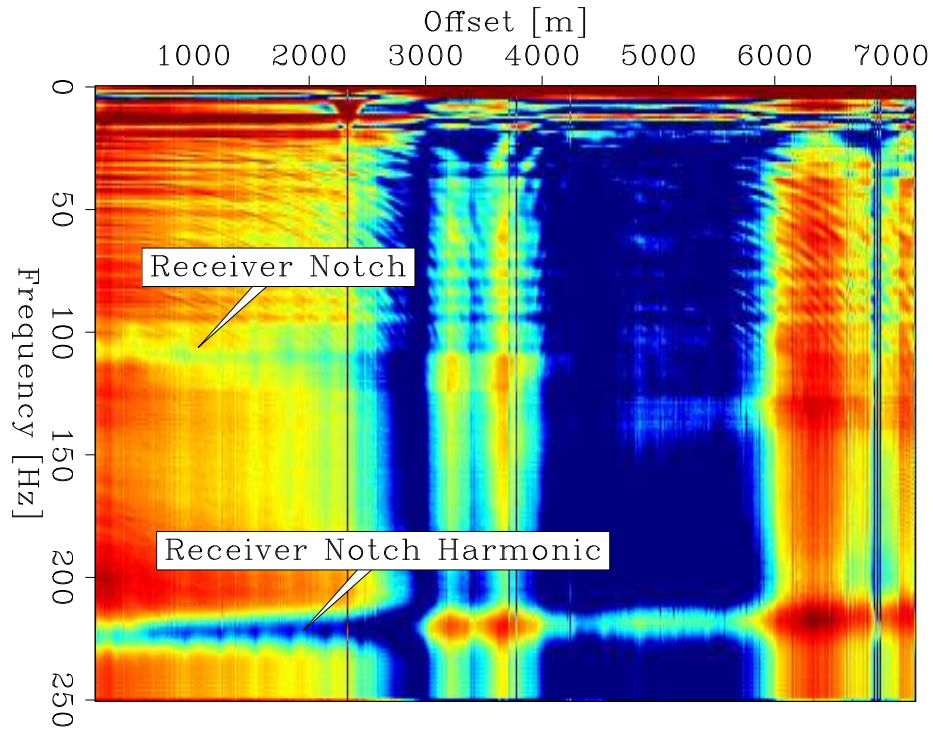
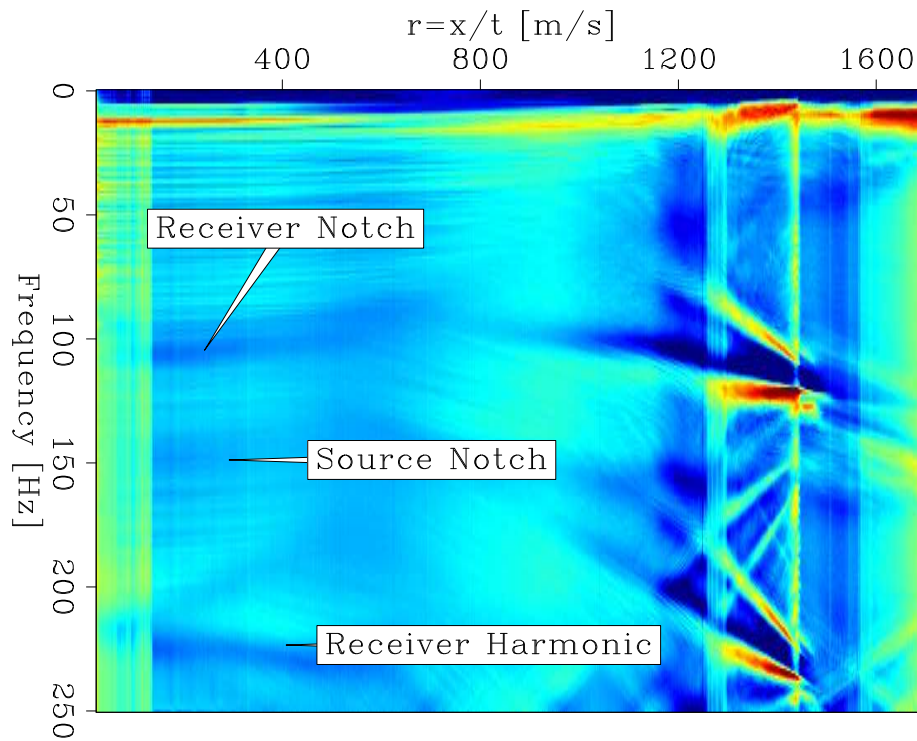


Figure 5: (a) Velocity-filtered data input. (b) After radial-domain transform. [ER]



(a)



(b)

Figure 6: Extracted wavelet spectra for: (a) (x,t) deconvolution, and (b) (r,t) deconvolution. [ER]

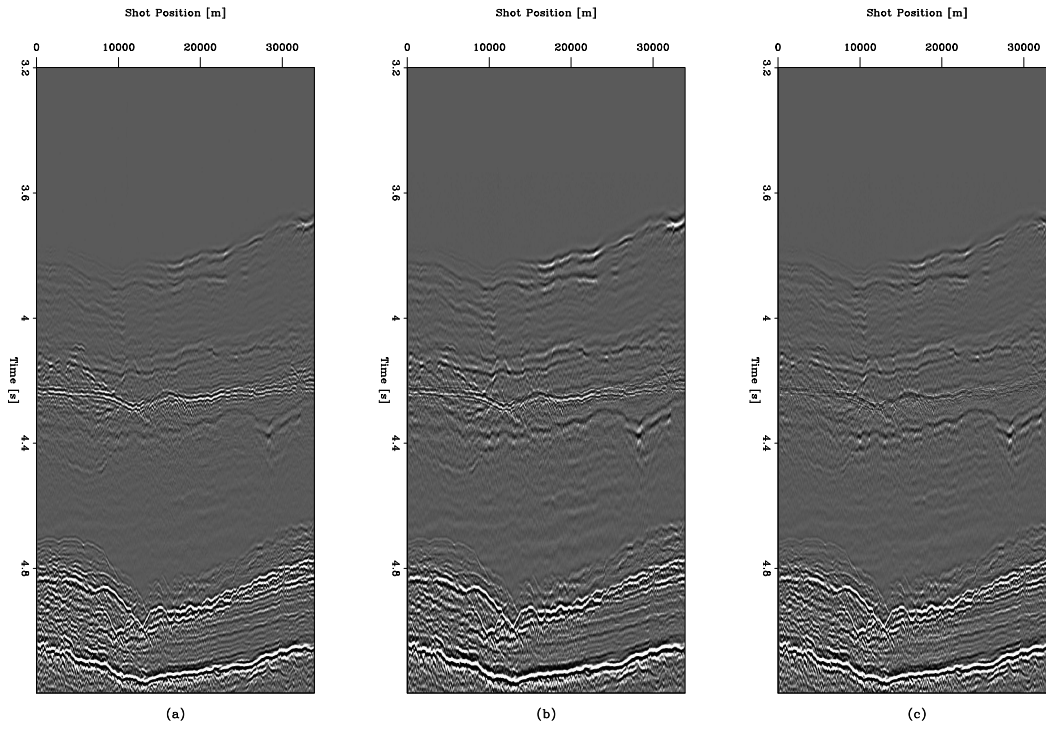


Figure 7: (a) (x,t) deconvolution: Dd . (b) Operator response: $R^{-T}R^T d$. (c) (x,t) deconvolution $(R^{-T} + \epsilon)DR^T d$. Offset = 6000 m. [CR]

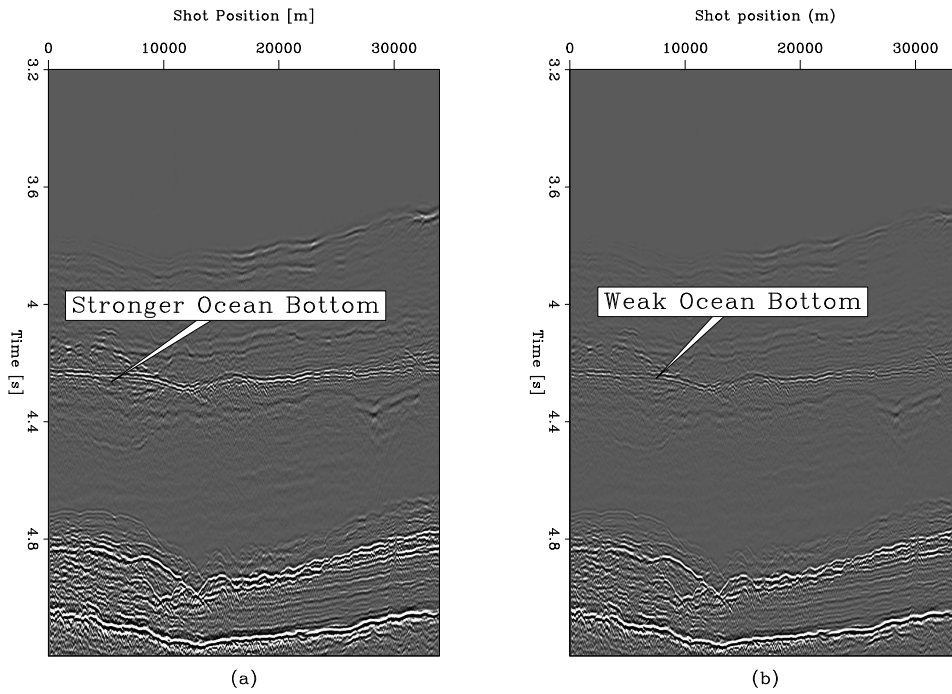


Figure 8: (a) (x,t) deconvolution: Dd . (b) Corrected (r,t) deconvolution: $R^{-T}DR^T d$. Offset = 6000 m. [CR]

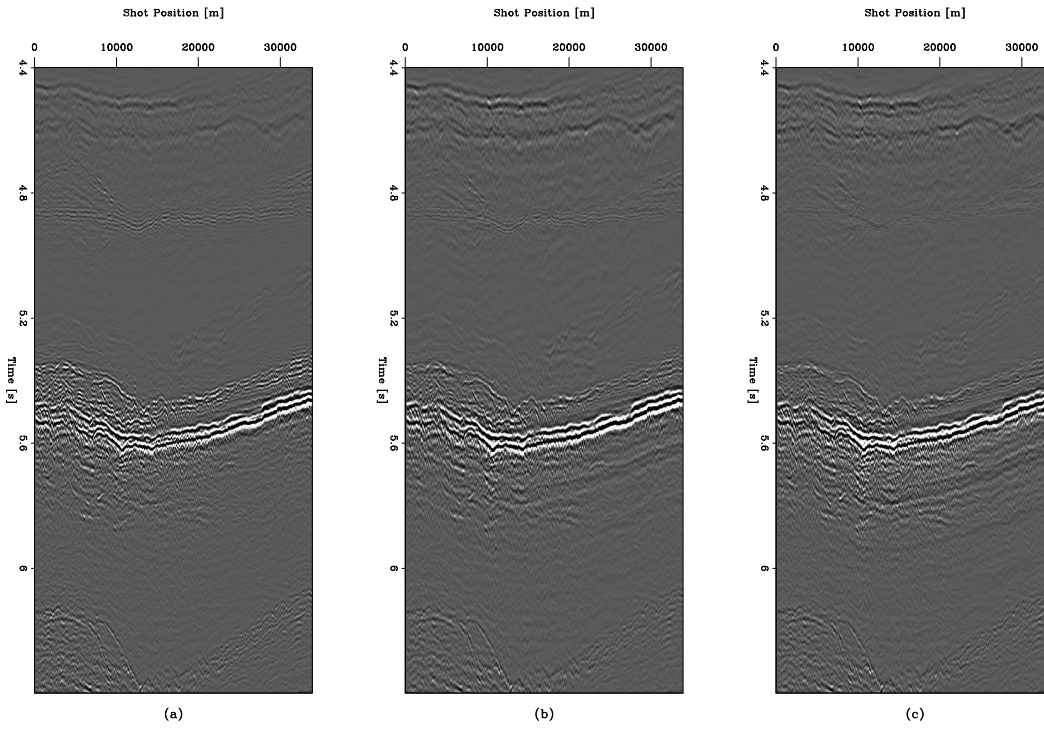


Figure 9: (a) (x,t) deconvolution: Dd . (b) Operator response: $R^{-T}R^T d$. (c) (x,t) deconvolution $(R^{-T} + \epsilon)DR^T d$. Offset = 7000 m. [CR]

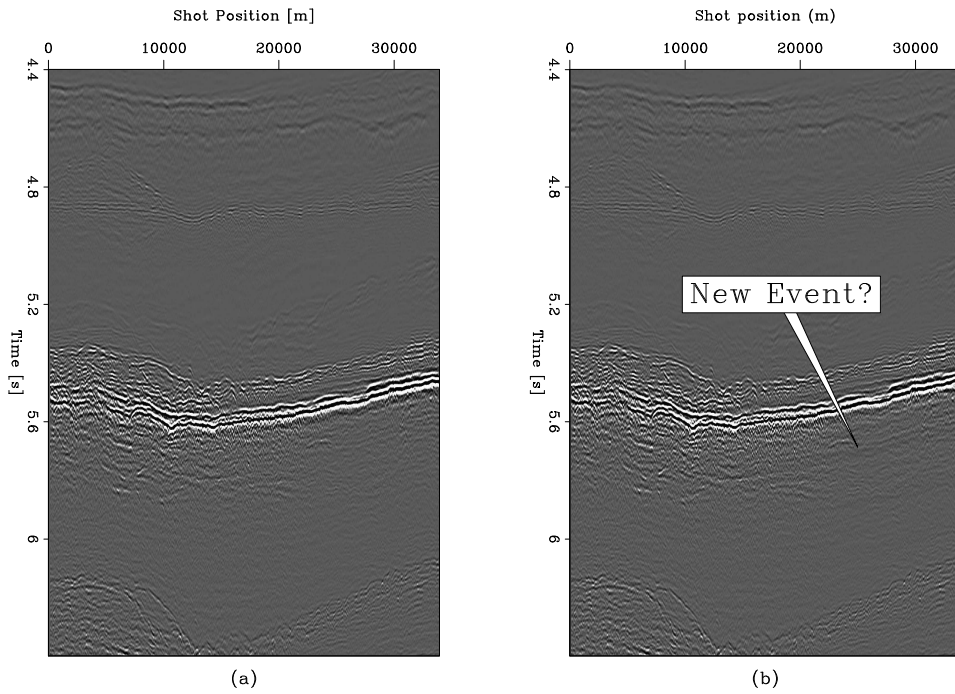


Figure 10: (a) (x,t) deconvolution: Dd . (b) Corrected (r,t) deconvolution: $R^{-T}DR^T d$. Offset = 7000 m. [CR]

DISCUSSION

Deconvolved Data

Once the velocity filter was applied to the data, both (x,t) and (r,t) domain deconvolution could be performed. For (r,t) deconvolution, the data was first transformed from the (x,t) domain to the (r,t) domain (Figure 5), and then deconvolution was performed along each common-angle panel. Likewise, in the (x,t) domain, deconvolution extracted the source wavelet from each common-offset panel. Since the geology is generally consistent horizontally, deconvolution along the common-offset and common-angle panels creates a filter that effectively averages the source wavelet across all shots. In order to compare the two methods, the (r,t) image cube was transformed back into the (x,t) space after deconvolution using a conjugate gradient solver.

Theory suggests that the low-velocity (low r value) traces will be similar to the near-offset traces, while the (r,t) transform differs most from the (x,t) at far offset. As a result, we expect to see the most significant difference between deconvolutional approaches in the far-offset areas of the shot gather, which is where the raypaths for the reflection events differ the most. For this reason, Figures 7 and 9 show offsets at 6000 m and 7000 m, respectively.

At far offset, deconvolution in the (x,t) domain is dominated by the stronger energy of the ocean-bottom reflection and head wave. This means the extracted wavelet will be best matched to this earlier, stronger energy. However, Figure 5 shows that the (r,t) transform shapes the reflection energy such that most of the traces in the new domain have similar time-lengths of reflection energy (for traces less than about $r=1000$ m/s). This means that for more traces, the first arrival/far-offset energy does not dominate in the deconvolution as much as it does in (x,t) space. The results of this are clear in Figures 10 and especially 8, where the earlier events in the (r,t) case are noticeably weaker than in the (x,t) case.

In side-by-side comparison, Figures 7 and 9 show that the image resulting from the response of the (r,t) transform is very similar to the final (r,t) image. When we correct for the response in the image due to the (r,t) transform and inversion, we get the results shown in Figures 8 and 10. These corrected (r,t) results confirm the general similarity between the (r,t) and (x,t) deconvolution methods that is implied in Figures 7 and 9.

These corrected (r,t) images with the operator response approximately removed are mathematically expressed by $I = F^{-1}DFd$, where $F = L'$ is the transform operator from (x,t) to (r,t) (thus the adjoint of L) and D is the deconvolution operator. However, since we use conjugate gradient methods to iteratively solve for the transform, what we really have is $I = (F^{-1} + \epsilon)DFd$, where ϵ represents the inherent error introduced from iteratively solving for the inverse of our forward operator. The following equations show how the effect of this error can be approximately removed.

We make the assumption that $\epsilon D F d \approx D \epsilon F d$, which is true when either ϵ or D is close to identity. Because the differences between the (r,t) deconvolution results and the operator response image is quite small, we allow the assumption of $D \approx I$.

$$\begin{aligned} I_{\text{response}} &= (F^{-1} + \epsilon) F d \\ &= (F^{-1} F d + \epsilon F d) \end{aligned} \qquad \begin{aligned} I_{\text{original}} &= (F^{-1} + \epsilon) D F d \\ &= (F^{-1} D F d + \epsilon D F d) \end{aligned}$$

$$\begin{aligned} I_{\text{residual}} &= d - I_{\text{response}} \\ &= d - (F^{-1} F d + \epsilon F d) \\ &= -\epsilon F d \end{aligned} \qquad \begin{aligned} I_{\text{correct}} &= I_{\text{original}} + D I_{\text{residual}} \\ &= (F^{-1} D F d + \epsilon D F d) - D \epsilon F d \\ &\approx F^{-1} D F d \end{aligned}$$

When we examine the differences between the common offset images at far offset (Figures 8 and 10), the improvements in illumination are virtually unobservable. In Figure 10 some new information is visible, but it is not clear whether this is in fact a hidden reflector that is now exposed, or if it is an artifact of the deconvolution. On the other hand, Figure 8 seems to have less illumination in the indicated areas. This reflector is the ocean bottom, and lies almost completely along the radial trace at water velocity. In the radial domain, any reflection that travels at water velocity will have close to zero frequency, and the prediction error filter in our deconvolution dampens it accordingly.

Extracted Wavelet Spectra

The extracted wavelet from the (r,t) deconvolution (Figure 6(b)) displays the expected frequency notches similarly to the wavelet extracted using (x,t) deconvolution (Figure 6(a)). While the (x,t) results only seem to show a receiver notch and its harmonic, the (r,t) results show the source frequency notch slightly better. One particularly interesting observation is that the “harmonic” receiver notch seems to curve in the opposite direction of the primary receiver notch. We suspect that this non-linearity is due to the (r,t) transform. Another feature found in the (r,t) results is the presence of numerous crossing “slants” at larger radial values (beyond the approximate critical angle), which remain to be thoroughly understood. More consistent with our observations is the primary receiver notch, which curves towards lower frequencies at increasing radial values. Since increasing radial values mean higher take off and arrival angle, this means longer ray paths through each layer, which translates into the attenuation and loss of higher frequencies that we observe.

FUTURE WORK (JON)

Different angles of propagation should require different deconvolution filters. This is mainly because the effective depth of burial of the gun and the hydrophones varies with propagation angle. The air bubble resonance, however, is an effect that we expect to be independent of propagation angle.

We see two straight forward ways to deal with the angle effect on deconvolution filters. The first (begun in this paper) is to use radial traces. The second (which we intend to explore) is to multiply each shot gather by a family of wedge-shaped weighting functions. One such weighting function is shown in Figure 11.

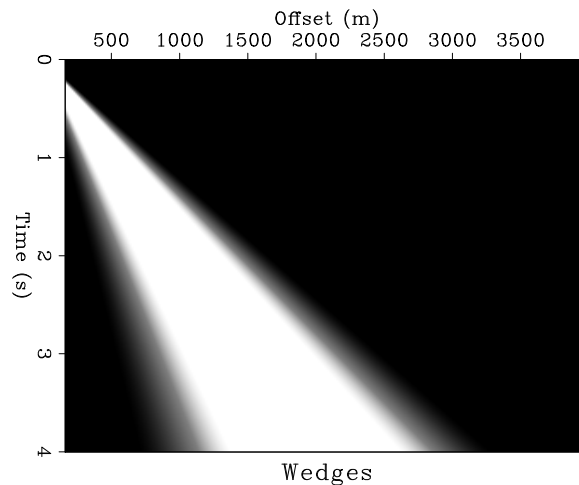


Figure 11: Wedge-shaped weighting function to select a zone of expected take-off and arrival angles. [NR]

More elaborate dip decompositions are possible (such as decomposition in the Fourier domain), but we shall begin with these two radial traces and a spectrum of weights such as in Figure 11.

Looking forward, the radial traces allow for rapid changes in angle but achieve statistical stabilization by averaging over shots (or midpoints). On the other hand, decomposition by zones has lower resolution by angle, but it achieves some statistical stabilization by averaging over many traces in a gather.

CONCLUSION

By performing deconvolution in the (r,t) domain, the assumptions implicit in the standard convolutional model are satisfied far better than with deconvolution in the (x,t) domain. However, results from 2D field data indicate very limited differences in the amplitude, polarity contrast, and sharpness of events, and in some cases demonstrate a reduction of reflector illumination. As we predict with our theory regarding ghost reflections, we find in both cases that the frequency notches at about 110 Hz and 150 Hz are visible at the nearest offset and angle, with the spectra from the (r,t) domain extracted wavelet displaying these notches similarly to the (x,t) domain case. While in theory the (r,t) deconvolutional method would be expected to offer a more

robust option for performing deconvolution, for this data set, the method does not seem to demonstrate any significant improvement in results.

ACKNOWLEDGMENTS

We want to thank Chevron for generously providing the data used in this paper. We also want to thank Antoine Guitton for the guidance and constructive criticism that he has provided throughout this work. He is also co-author of some of the programs used for the deconvolution steps.

APPENDIX (JON)

Air Gun Sources Lack Low Frequencies

Since raw marine data often shows sea swell with frequencies commonly as low as 0.1 Hz, it is tempting to conclude that low-frequency signal is present. It is not. The recorders record it, but the guns do not send it. The only signal we have at low frequencies is what we might be able to unscramble from the ambient noise. To see what is in the Chevron Australia data set, we applied a high-cut filter at 5 Hz. Figure 12 shows hardly anything left. At a little lower cutoff frequency it would not be possible to detect hyperbolic continuity.

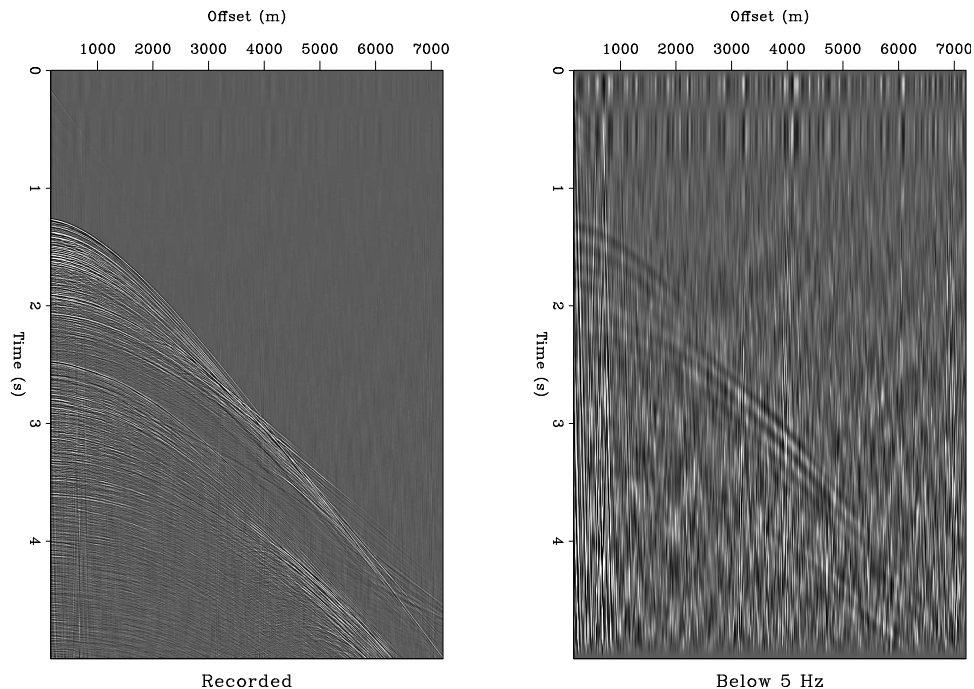


Figure 12: Data quality is poor at low frequencies. If the cut-off frequency is below about 5 Hz it is not possible to see the hyperbolic continuity. [NR]

For those of us hoping to estimate earth impedance, this is a sad state of affairs. One of us (Jon) advocates investigating the water cannon as a source. With such a source, one shoots water up into the sky. The water falls back to the surface only after data has been recorded.

If our goal is impedance estimation, we must have low frequencies. What are our alternatives?

1. Deeper guns
2. Water cannon source
3. Learn to use ambient noise as source. (Unfortunately, we don't have a surface receiver array suitable to destruction of water waves from all sides.)

REFERENCES

- Barak, Claerbout, G. R., 2012, Decon in the log domain - practical considerations: SEP, **148**, 19–34.
- Claerbout, 2013, Low-velocity deconvolution.
- Guittou, C., 2012, Six tests of sparse log decon: SEP, **148**, 35–48.
- Henley, 2004, More processing in the radial trace domain: 2004 CSEG National Convention: Great Explorations - Canada and Beyond, **148**, 1–4.
- Liner, C. L., 2004, 3D seismology, 2 ed.: PennWell Books.
- Margrave, S., 1997, An approach to nonstationary deconvolution.
- Zhang, Claerbout, G., 2011, A new bi-directional sparse/spike deconvolution method that overcomes the minimum phase assumption: SEP, **143**, 271–282.